

Total Scale: Face-to-Body Detail Reconstruction from Sparse RGBD Sensors

Zheng Dong¹ Ke Xu² Ziheng Duan¹ Hujun Bao¹ Weiwei Xu^{*1} Rynson W.H. Lau²

¹State Key Lab of CAD&CG, Zhejiang University ²City University of Hong Kong

zhengdong@zju.edu.cn, kkangwing@gmail.com, iduanziheng@gmail.com, {bao, xww}@cad.zju.edu.cn, Rynson.Lau@cityu.edu.hk

Abstract

While the 3D human reconstruction methods using Pixel-aligned implicit function (PIFu) develop fast, we observe that the quality of reconstructed details is still not satisfactory. Flat facial surfaces frequently occur in the PIFu-based reconstruction results. To this end, we propose a two-scale PIFu representation to enhance the quality of the reconstructed facial details. Specifically, we utilize two MLPs to separately represent the PIFus for the face and human body. An MLP dedicated to the reconstruction of 3D faces can increase the network capacity and reduce the difficulty of the reconstruction of facial details as in the previous one-scale PIFu representation. To remedy the topology error, we leverage 3 RGBD sensors to capture multiview RGBD data as the input to the network, a sparse, lightweight capture setting. Since the depth noise severely influences the reconstruction results, we design a depth refinement module to reduce the noise of the raw depths under the guidance of the input RGB images. We also propose an adaptive fusion scheme to fuse the predicted occupancy field of the body and face to eliminate the discontinuity artifact at their boundaries. Experiments demonstrate the effectiveness of our approach in reconstructing vivid facial details and deforming body shapes, and verify its superiority over state-of-the-art methods.

1. Introduction

Three-dimensional reconstruction of humans, which aims to obtain a dense surface geometry from single-view or multi-view human images, is a fundamental topic in computer vision and computer graphics. While high-fidelity 3D human models can be reconstructed using commercial multi-view stereo software under the customized studio setting [7, 16, 34, 50, 53], it is highly desirable to lift the studio setting constraint that is hard to access by users. Low-cost RGBD sensors are recently popular in 3D human reconstruction, and tracking-based methods have been developed to fuse the depth data from RGBD sensors as the recon-

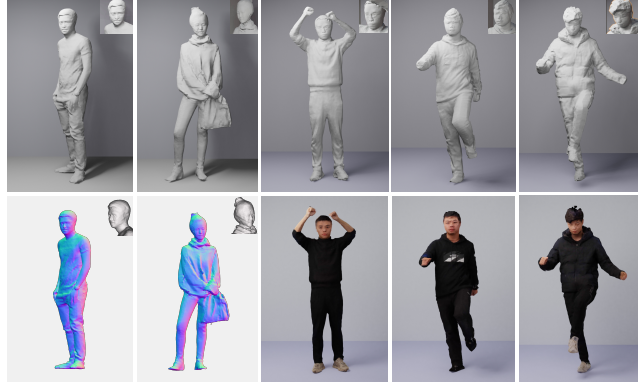


Figure 1. Our volumetric capture results with the high-fidelity body and face-enhanced details from three groups of raw RGBD images. First two columns: geometric and normal results on our testing dataset. Last three columns: geometric and textured results from our real shots.

struction results [41]. During fusion, the estimation of non-rigid human body deformation is essential to improve the reconstruction quality [40, 64]. However, it is technically challenging to guarantee the stability of the depth fusion algorithms due to occlusions and severe noises in the depth data.

Learning-based 3D human reconstruction methods can significantly simplify the capture setting. After training on high-quality 3D human models, they can even recover 3D human shapes from single images [25, 67]. The focus of learning-based 3D human reconstruction methods has been shifted from parametric human model [36, 43] to pixel-aligned implicit function (PIFu) representation [45]. As demonstrated in [45], different types of details, such as hair and clothing, can be reconstructed using PIFu from images. However, topology errors in the reconstructed human models often occur in the regions invisible in the input images. PIFuHD [46] synthesized the normal maps for a captured human image at both frontside and backside, which can partially remedy the topology errors. However, the details reconstructed from the synthesized normals might not be consistent with the target. Through a carefully designed multi-view feature fusion scheme, the topology error of the reconstructed human model can be significantly reduced [22, 63]. While PIFu-based methods developed

*Corresponding author.

fast, we observe that the quality of reconstructed details is still not satisfactory. For instance, flat facial surfaces frequently occur in the PIFu-based reconstruction results. It is technically challenging for PIFu-based methods to achieve high-fidelity detail reconstruction results without topology errors.

In this paper, we propose a two-scale PIFu representation to enhance the quality of the reconstructed facial details. Specifically, we utilize two MLPs to represent the PIFus for the face and human body separately. It is inspired by the fact that the complexity of a function can be reduced when observing it locally. Thus, we expect that a separate MLP for the reconstruction of 3D faces can increase the network capacity and reduce the difficulty of reconstructing facial details as in the previous one-scale PIFu representation. Moreover, we propose an adaptive fusion scheme to fuse the predicted occupancy field of the body and face to eliminate the discontinuity artifact at their boundaries. Additionally, to address the topology issue, we leverage 3 RGBD sensors to capture multiview RGBD data as the input to the network, a sparse, lightweight capture setting. Since the depth noise severely influences the reconstruction results, we design a depth refinement module to reduce the noise of the raw depths under the guidance of the input RGB images. As illustrated in Fig. 1, our method can generate reconstruction results with the high-fidelity body and enhanced facial details for different actions.

In summary, the main contributions of our work are:

- We propose a two-scale PIFu representation to reconstruct 3D humans from very sparse RGBD inputs. Moreover, a novel depth refinement module is incorporated into our network to reduce noise and improve reconstruction details under the supervision of the differentiable surface reconstruction module.
- Extensive experiments show that the proposed human total reconstruction model can obtain high-quality body reconstruction results, especially face, under the noisy depth maps taken by the Kinect sensors.

2. Related Work

Tracking-based Human Reconstruction. A line of human reconstruction methods [4, 5] is tracking-based, which leverage the pre-captured mesh templates [17–19, 29, 72] or temporal fused mesh [28, 40, 41, 48, 64] as the reference model and track the human motions by inferring the deformations of the reference model. Some methods [3, 15, 19, 32, 59, 62, 64] are proposed to use 3D pose to parameterize the reference model, while others [21, 23, 44, 61, 64, 65] typically leverage the parametric body model SMPL or SMPL-X [36, 43]. Furthermore, Hanbyul *et al.* [24] constructed parametric models for the human face, body, and hand to improve the reconstruction results. Liu *et al.* [35] propose

to combine image segmentation and tracking with 3D shape prior to multi-person reconstruction. Similarly, Mustafa *et al.* [38] leverage the segmentation with the optical flow to reconstruct humans in dynamic scenes. To tackle the occlusion and large motion problems, some methods develop high-end capture systems for the dense capture of human performance, which consist of a large number (up to 100) of RGBD sensors [7, 34, 50] or custom color lights [16, 53] (*e.g.*, there are 1200 individually controllable light sources in the acquisition setup in [53]).

Learning-based Human Reconstruction. Another line of methods [1, 14, 39, 47, 51, 55, 60, 70, 71] is learning-based, which leverage the advanced neural 3D representations for reconstructing the geometry and/or texture details. Some methods proposed to reconstruct 3D human meshes from a single RGB [47] or RGBD [55] image, by incorporating the SMPL [49, 70]. To avoid being constrained to the SMPL template, some methods adopt the image-to-image translation pipeline to regress the input image into 3D meshes via 2D estimations of intermediate textures [1], silhouettes [39], and depth information [14], while others jointly exploit the 2D and 3D information, *e.g.*, body joints and per-pixel shading information [71], and 2D/3D poses and segmentation map [51]. However, these methods typically suffer from over-smoothed surfaces in the occluded regions. Some methods [10, 11, 31] propose to leverage multi-view RGBD images for high-frequency detail reconstruction.

Recently, the pixel-aligned implicit function (PIFu) [45] has attracted much attention, as this implicit representation enables a direct infer of 3D object surfaces and textures from the 2D image pixels. Saito *et al.* [46] propose to estimate the front and back normal maps to reduce the geometry errors of PIFu in the occluded regions. The success of PIFu in detail reconstruction drives many methods to combine it with parametric model [56, 66] and semantic segmentation [12], camera parameters estimation [27], novel view synthesis [30], single-view [31] or multi-view depth information [63], or apply it for point clouds based human reconstruction [2, 6, 37].

Our method tackles the limitation of lacking facial details of PIFu-based methods by learning a two-scale PIFu representation, enhancing our network capacity to reconstruct the geometric details at all scales.

3. Method

Our proposed face-to-body neural human reconstruction network is a two-stage network, as illustrated in Fig. 2. Given raw RGBD images from N (*e.g.*, three) perspective views, our network can reconstruct a full-body human model with the face-enhanced details by leveraging the proposed depth refinement module (RDM) and the face-to-body neural surface estimation module (FBSM). In general, our system performs the following three steps sequentially:

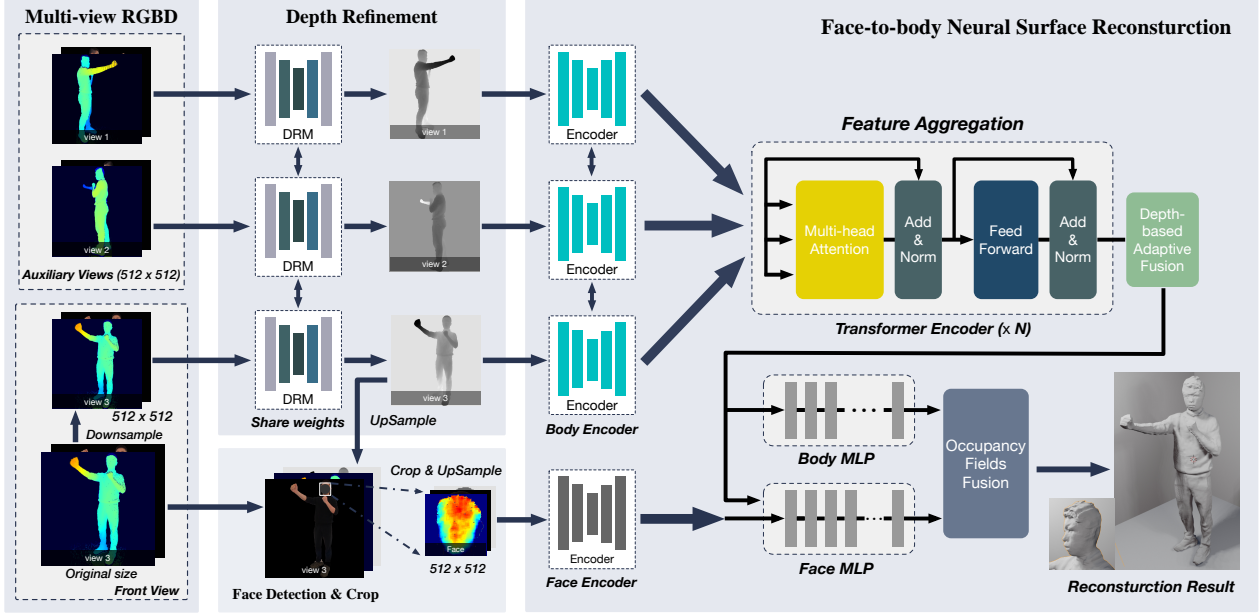


Figure 2. Overview of our face-to-body neural human reconstruction network architecture. “ $\times N$ ” indicates that the transformer encoder is repeated N times. Depth Refinement: predict the refined depth maps of the raw depth maps with the guidance of RGB inputs. Face-to-body Neural Surface Reconstruction: predict the occupancy fields for the human body and face independently based on pixel-aligned depth and RGBD features, then integrate the two inferred fields to generate a complete model with high-quality details.

1) **Depth Refinement.** Given the full-body portrait (RGB) with binary mask and the raw aligned depth map as inputs, we design a contextual auto-encoder to obtain the refined depth with the guidance of the full-body portrait.

2) **Face-to-body Neural Surface Reconstruction.** To reconstruct the body along with the face-enhanced details, we design two pixel-aligned implicit functions for face and body, respectively, *i.e.*, the two-scale PIFu representation for the 3D human. For the body part, a PIFu \mathcal{F}_b , called *PIFu-Body* receives refined depth maps from N views as inputs and predicts the occupancy field of the body part. For the facial part, we first detect and crop the human face from the designated front-view RGBD body portrait of the original resolution. Afterward, we design a light-weighted network as another PIFu \mathcal{F}_f , called *PIFu-Face*, to predict the occupancy field for the face according to the features learned from the up-sampled RGBD face image.

3) **Face-to-body Occupancy Fields Fusion.** We design an adaptive occupancy fields fusion scheme during inference to get a complete model with a smooth transition between face and body occupancy fields. Specifically, for the queried points projected on the face region, we calculate their projected signed distance function (PSDF) values through the refined front-view facial depth map and construct Gaussian probability distributions to weigh the occupancy values of the two fields. The PSDF value is defined as the difference between the depth component of a 3D point and its depth value obtained at its projection in a depth map [8, 32]. Finally, we produce the global mesh through the marching

cube algorithm.

3.1. Depth Refinement

Since the captured depth maps from consumer-level cameras have non-negligible noises and holes, directly utilizing the raw depth maps for static reconstruction will introduce the noises into the final results. Therefore, we propose a Depth Refinement Module (DRM) to reduce the sensor noises and refine the eroded boundaries of the input raw depth map with the guidance of RGB body portrait as inputs. This design also provides relatively cleaner depth inputs for our FBSM.

The network structure of our DRM is shown in Fig. 3. For clarity, we denote RGB body portrait as \mathbf{I} , the corresponding binary body mask as \mathbf{M} obtained by the background-matting method [33], \mathbf{D}_{raw} as the normalized result of the captured depth map, and the refined depth map as \mathbf{D}_{rf} , where $\mathbf{D}_{rf} = \text{DRM}(\mathbf{D}_{raw}, \mathbf{I})$. The architecture with two different types of inputs, *i.e.*, \mathbf{I} and \mathbf{D}_{rf} , is inspired by the hypercolumn structure in [20] and DDR-Net [60]. Correspondingly, we design a contextual auto-encoder with two encoding branches to fill the \mathbf{D}_{raw} ’s holes and add high-frequency details from \mathbf{I} to the refined depth map \mathbf{D}_{rf} .

We input \mathbf{I} and \mathbf{D}_{raw} to the two branches of the encoder in DRM so as to extract texture and depth features. After each branch’s last *Conv* layers, the network fuses these two types of features in an additive manner, a late fusion scheme to fuse RGB and depth information. Since we use fewer

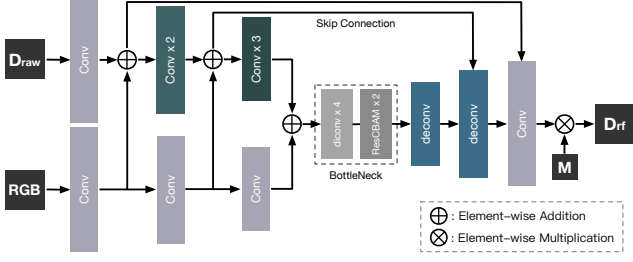


Figure 3. The structure of our Depth Refinement Module. “ $M \times N$ ” indicates that the module M is repeated N times. ResCBAM: the ResBlock with CBAM (Convolutional Block Attention Modules [58]).

Conv layers to extract textured features, it also makes high-level depth features contain more original high-frequency details, leading to a lighter encoder. In the bottleneck layers of the encoder, we first use four dilated *Conv* layers with different scales to extract global features, and then additionally leverage non-linear CBAM (Convolutional Block Attention Module) [58] blocks to compute the channel-wise and spatial attention. The decoder part upsamples the encoded depth feature to the original size, together with the skip connections to preserve depth details in D_{raw} . Finally, we multiply the mask M by the output of the last *Conv* layer of the decoder to get the refined depth map D_{rf} , resulting in zero values inside the background regions.

Training Loss. We render the ground-truth depth map, denoted as D_{gt} from a model in our training dataset. The first loss L_{depth} is used to penalize the per-pixel difference between D_{rf} and D_{gt} :

$$L_{depth} = \|D_{rf} - D_{gt}\|_1 + \|D_{rf} - D_{gt}\|_2.$$

However, we observe that this loss alone might lead to blurring in the refined depth map.

To this end, we introduce a *normal loss*, denoted as L_{nor} , to measure the difference between the normal maps computed from the predicted and the ground-truth depth maps, denoted by N_{rf} and N_{gt} respectively. In addition, we combine it with SSIM (structural similarity index) [57] loss to improve the details in the predicted results:

$$L_{nor} = \beta \mathcal{L}(N_{rf}, N_{gt}) + (1 - \beta) L_{SSIM}(N_{rf}, N_{gt}),$$

where the weight β is set to 0.16, following the design in [68]. \mathcal{L} is the smooth l_1 loss. The normal maps are calculated at each pixel according to the difference among its four surrounding pixels, a differentiable operation.

The final training loss for our DRM is then defined as:

$$L_{DRM} = \lambda_1 L_{depth} + \lambda_2 L_{nor},$$

where λ_1 and λ_2 are the weights to balance the two terms.

In addition to the designed loss L_{DRM} , D_{rf} is also supervised by the loss terms used in FBSM, since D_{rf} is the input of our differentiable FBSM and the back-propagated gradient will flow through D_{rf} to DRM. Such a design

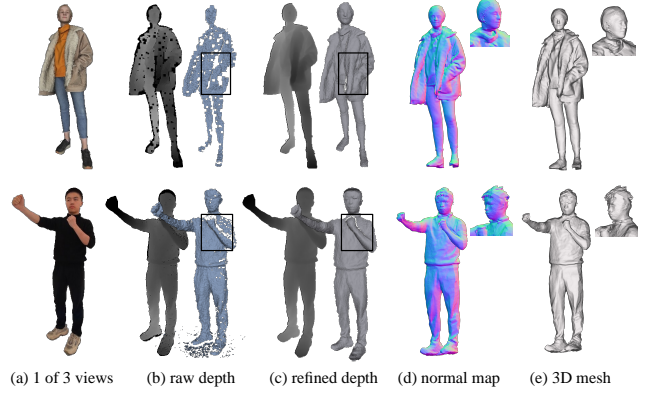


Figure 4. Our depth refinement result on single view depth map and the subsequent reconstruction results.

makes L_{DRM} decline faster during joint training. The mean absolute error (MAE) for each pixel of our DRM results on our testing dataset is 0.0769cm. To simulate the RGBD sensor data, we synthesize the depth noises of D_{raw} and impose the noise on D_{gt} . As shown in Fig. 4, our DRM can effectively refine the raw depth map with eroded boundaries and holes (black-boxes), leading to better reconstruction results using our FBSM.

3.2. Face-to-body Neural Surface Reconstruction

Although the refined multi-view depth maps $\{D_{rf}\}_i (i = 1, \dots, N)$ output by the DRM can be fused (e.g., TSDF-Fusion in [41]) to obtain a 3D human model, the reconstructed mesh in this way contains large holes and low-quality regions due to the very sparse inputs and the self-occlusions. Therefore, we design a face-to-body neural surface estimation Module (FBSM), as shown in Fig. 5, to generate high-fidelity reconstruction results. This module consists of two-scale PIFus: PIFu-Body for the body part and PIFu-Face for the facial details. The PIFu-Body takes the multi-view depth maps as the input and predicts the volumetric occupancy field for the whole body, while the PIFU-Face takes both RGB and depth map cropped from the front-view RGBD image as the input and predict the volumetric occupancy field for the 3D face. Finally, these two occupancy fields are adaptively fused to reconstruct the final 3D human mesh. In the following, we first introduce some notations and then proceed to the details of PIFu-Body and PIFu-Face, multi-view feature aggregation, the fusion of two predicted occupancy fields, and the training of the two-scale PIFus.

Notation: Let us denote a 3D point in the bounding box of a human body as \mathbf{X} , and its 2D projection \mathbf{x}^i at i -th view as $\mathbf{x}^i = \pi^i(\mathbf{X})$, where π^i is the projection function. The symbol $\mathbf{z}^i = z(\mathbf{X}^i)$ is used to denote the depth of \mathbf{X} in the local coordinate system of the i -th view, and $p^i(\mathbf{X})$ is the truncated-PSDF, where $p^i(\mathbf{X}) = T(\mathbf{z}^i - S(\mathbf{x}^i; D_{rf}^i))$. The

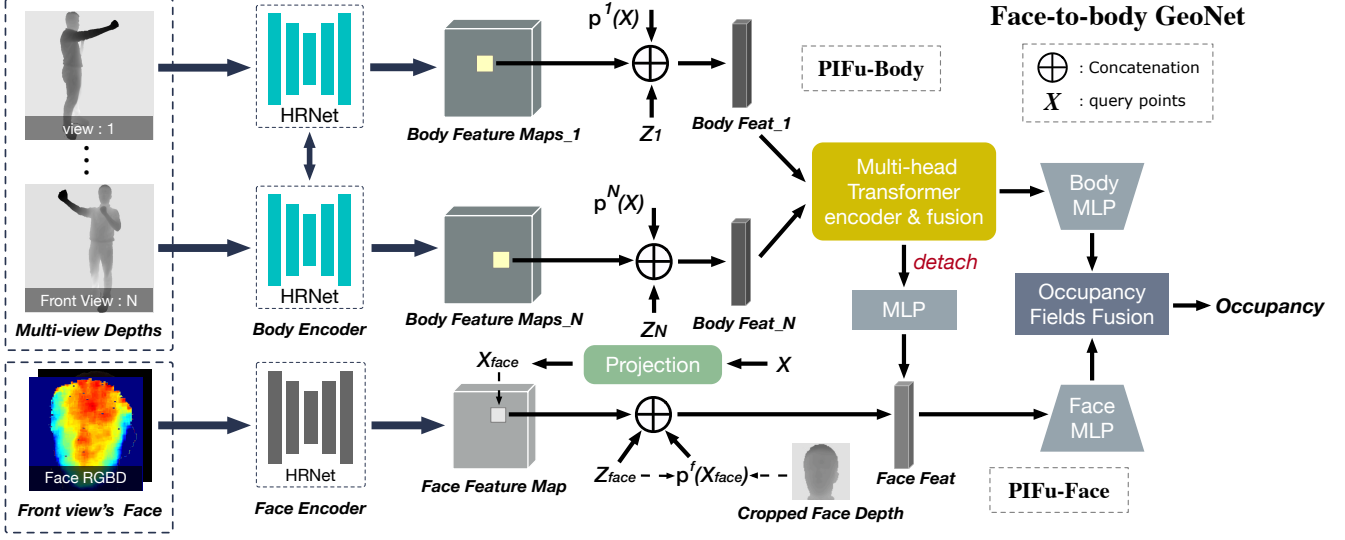


Figure 5. The architecture of our Face-to-body Neural Surface Estimation Module (FBSM).

symbol $S(\mathbf{x}^i; \mathbf{D}_{rf}^i)$ represents a bi-linear sampling function used to retrieve the depth value from \mathbf{D}_{rf}^i at \mathbf{x}^i , and $T(\cdot)$ is used to truncate the PSDF values in $[-\delta_p, \delta_p]$ [63]. For the input RGBD images, we employ HRNet [54] as the backbone to extract pixel-aligned features. The HRNet for multi-view depth maps in PIFu-Body is denoted as \mathcal{H}_b , and \mathcal{H}_c denotes the HRNet for PIFu-Face. Two MLPs are used to represent the volumetric occupancy fields of human body and face, denoted by \mathcal{M}_b and \mathcal{M}_f respectively. Finally, the detected facial regions in the front-view RGBD image is denoted as \mathbf{R}_f .

PIFu-Body. \mathcal{F}_b can be formulated as follows:

$$\mathcal{F}_b(\mathbf{X}, \mathbf{D}_{rf}) = \mathcal{M}_b(\mathcal{A}(S(\mathbf{x}^i, \mathcal{H}_b(\mathbf{D}_{rf}^i), c^i(\mathbf{X})))_{i=1, \dots, N})),$$

where one of the input to \mathcal{A} is $c^i(\mathbf{X}) = [\mathbf{z}^i, p^i(\mathbf{X})]$. It is a concatenation of local depth and Truncated-PSDF of \mathbf{X} as in [63]. The original resolution of \mathbf{D}_{raw} when training is 2048×2048 , but reduced to 512×512 after aligning it to the RGB image as the input of our DRM, which results in the resolution 512×512 of \mathbf{D}_{rf} . The symbol \mathcal{A} indicates the multi-view feature aggregation module (see details below).

PIFu-Face. \mathcal{F}_f can be formulated as follows:

$$\mathcal{F}_f(\mathbf{X}_f, \mathbf{Q}_f) = \mathcal{M}_f(S(\mathbf{x}_f; \mathcal{H}_f(U^\uparrow(\mathbf{Q}_f))), \mathbf{f}_b, c(\mathbf{X}_f)),$$

where $\mathbf{Q}_f = [\mathbf{I}_f, \mathbf{D}_f]$ is the raw facial RGBD input cropped from the front-view RGBD images, to prevent the loss of facial details, and U^\uparrow indicates the up-sampling operation, increasing the resolution of \mathbf{Q}_f to the same resolution as \mathbf{D}_{rf} . The \mathcal{M}_f also takes the feature \mathbf{f}_b from \mathcal{H}_b as input, since \mathbf{f}_b can provide context information for facial regions. PIFu-Face is trained only using the 3D point \mathbf{X}_f near the face, and \mathbf{x}_f is its projection to the front-view. The input

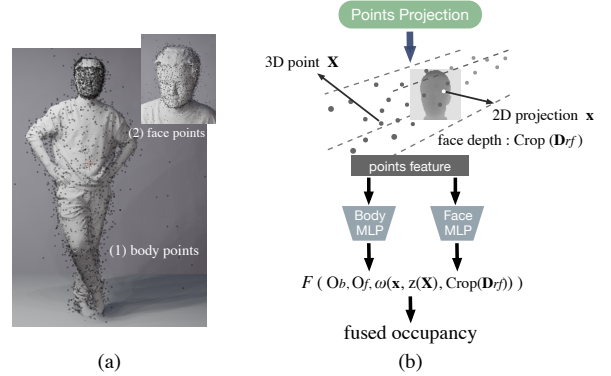


Figure 6. 3D point sampling and occupancy fusion. (a) 3D point sampling for the training. The number of sampled 3D points around the face equals the number of sampled body points. (b) Occupancy fusion during inference.

depth information $c(\mathbf{X}_f)$ is defined in the same way with PIFu-Body, but the truncated-PSDF value is computed using the cropped \mathbf{D}_{rf} to reduce noises. The RGB image of the facial region is beneficial to enhance the reconstructed facial details.

Multi-view Feature Aggregation Module \mathcal{A} . It is inspired by the attention mechanism in [52] and the transformer-based feature fusion methods in [63, 69]. Specifically, we first adopt the transformer encoder with multi-head self-attention layers to denoise the features using attention weights sampled from multi-view feature maps for a query point \mathbf{X} . Besides, we observe that the attention mechanism can avoid over-blurred features in the denoising. Our implementation uses multi-head attention with four heads and two linear layers in the transformer.

After the feature denoising, we introduce a depth-based adaptive feature fusion method to aggregate the features $\mathbf{a}_i (i = 1, \dots, N)$ output by the transformer encoder. For

a 3D point \mathbf{X} , we first calculate $p^i(\mathbf{X})$ at i -th view, and then linearly combine the features according to the fusion weights: $\exp(-\sigma_0 \cdot (p^i(\mathbf{X}))^2)$, where σ_0 is a factor to control the degree of aggregating (default 20).

Face-to-body Occupancy Fields Fusion. During inference, two occupancy fields must be fused to eliminate the discontinuity artifacts at their boundaries. For a 3D point \mathbf{X}_f projected to the detected facial region \mathbf{R}_f in the front view, we first calculate its 2D projection \mathbf{x}_f located between $[-1, 1]$ in normalized image coordinates and then its PSDF value $p^f(\mathbf{X}_f)$. These two quantities are used to compute weights using a mixture of Gaussian distributions:

$$\omega = \exp(-\sigma_1 \cdot \|\mathbf{x}_f\|^2) \cdot \exp(-\sigma_2 \cdot (p^f(\mathbf{X}_f))^2),$$

where the first component is larger at the center of facial region and decrease smoothly to the boundary. It is used to improve the smoothness of the fused occupancy field around the boundary. The second component emphasizes the occupancy value computed by PIFu-Face according to $p^f(\mathbf{X}_f)$. Two weights, σ_1 (default 1) and σ_2 (default $1e^3$), are used to control the fusion degree for two fields. Finally, we can leverage ω to fuse the two inferred occupancy values: O_b, O_f output by PIFu-Body and PIFu-Face respectively. The fusion operation is defined as $F(O_b, O_f, \omega) = \omega \cdot O_f + (1 - \omega) \cdot O_b$, as shown in Fig. 6.b.

Training Loss. We adopt the extended Binary Cross Entropy (BCE) loss [46, 70] to train our FBSM on the sampled points $\tilde{\mathbf{X}} = [\mathbf{X}_b, \mathbf{X}_f]$:

$$L_O = \alpha_0 \sum_{\mathbf{X}_b \in \mathcal{S}_0} L_{BCE}(O_b, O_b^*) + \alpha_1 \sum_{\mathbf{X}_f \in \mathcal{S}_1} L_{BCE}(O_f, O_f^*),$$

where O_b^* and O_f^* are the ground-truth occupancy values of the 3D points $\tilde{\mathbf{X}}$ of human body and face respectively, \mathcal{S}_0 and \mathcal{S}_1 denote the sets of samples, L_{BCE} represents the BCE loss, α_0 and α_1 are the weights to balance PIFu-Body and PIFu-Face.

Given $\{\mathbf{D}_{rfj}\}_i (i = 1, \dots, N)$, \mathbf{Q}_f and the 3D query point \mathbf{X} , we jointly train these two-scale PIFus. We first sample 3D points near the surface and inside the bounding box of the ground-truth scan, according to PIFuHD [46]. For facial point, we obtain the 2D projection \mathbf{x}^f and the depth $\mathbf{z}^f = z^f(\mathbf{X})$ of \mathbf{X} in the front view: f . With the rendered ground-truth facial depth $\mathbf{D}_{gt}^c = \text{Crop}(\mathbf{D}_{gt})$ of the front view, we can set a flag $v^f(\mathbf{X})$ to mark face point for \mathbf{X} through \mathbf{R}_f and the absolute PSDF value as follows:

$$v^f(\mathbf{X}) = \begin{cases} 1 & \mathbf{x}^f \in \mathbf{R}_f \ \& \ \text{abs}(\mathbf{z}^f - S(\mathbf{x}^f; \mathbf{D}_{gt}^c)) < \tau \\ 0 & \text{else} \end{cases}.$$

When computing the training loss, we will replace the $\mathcal{F}_b(\mathbf{X})$ with $\mathcal{F}_f(\mathbf{X})$ if $v^f(\mathbf{X})$ is 1. It means that we expect the gradients of the 3D points on the face to flow through the \mathcal{F}_f such that \mathcal{F}_f can not be ignored in the training. In order to balance the training of the PIFu-Body and the PIFu-Face,

we sample the same number of 3D points on face and body simultaneously, as illustrated in Fig. 6.a.

4. Experiments

In this section, we report implementation details, how we prepare the training dataset, comparisons as well as the ablation studies of our method.

Implementation Details. We implement our two-scale PIFus using PyTorch [42] on a PC with two Nvidia Geforce RTX 3090 GPU. To minimize the loss terms for our DRM and FBSM, we adopt ADAM optimizer [26] to train our network for 30 epochs with a learning rate starting from $1e^{-4}$ and use an exponential learning rate scheduler to update it every 10 epochs by multiplying with the factor 0.1. The batch size is set to be 6. The β_1 and β_2 in ADAM are set to 0.5, 0.99, respectively. The network weights are initialized using a normal distribution (mean:0, variance: 0.02). The λ_1 and λ_2 appeared in our L_{DRM} are set to 1, 2, respectively. And we set δ_p as 0.01m, τ as 0.15m, α_0 and α_1 as 1 in our FBSM.

For \mathcal{H}_b in PIFU-Body, we follow [30, 63] to use HRNetV2-W18-Small-v2 [54] as the backbone. The resolution of its output feature map is 128×128 , and the number of channels is 128. In particular, we reduce the channel number of the inner blocks of \mathcal{H}_f of PIFu-Face to 2/3 of the original. For the transformer encoder, we set the repeated number N to 4. As for \mathcal{M}_b and \mathcal{M}_f , we use multi-layer perceptron (MLP) with skip connections [45, 46, 63] and set the channels dimension of hidden layers as (512, 256, 128, 128), (128, 128, 64, 64, 64), respectively.

We adopt three-view RGBD images with an interval of (135 degree, 135 degree, 90 degree) as the capture setting. The user is required to face the camera in the middle, *i.e.*, front-view f . The real depth data is captured using Microsoft Kinectv4 sensors with the same camera pose parameter settings. The captured RGB resolution is 2560×1440 and depth image resolution 1024×1024 . During testing, we use background-matting-v2 [33] to obtain the mask \mathbf{M} of body portraits and then use RetinaFace [9] to detect the front face for the front-view. It takes about 3.57s for our model (32-bit floating-point precision) to predict the occupancy field of resolution 256 with the given inputs.

Training Dataset. We use the THuman2.0 dataset from [63] as our training dataset, which contains 500 high-quality 3D human scans with various poses and cloth styles. First, we rotate each scan at 6-degree intervals on the yaw axis. Then we render RGB body portraits with an image resolution of 512×512 with CUDA acceleration based on the assumption that the body surface is mainly Lambert material, we also apply random shifts to augment the rendered results. Afterward, we render the ground-truth depth maps aligned with body portraits as \mathbf{D}_{gt} and synthesize the sen-

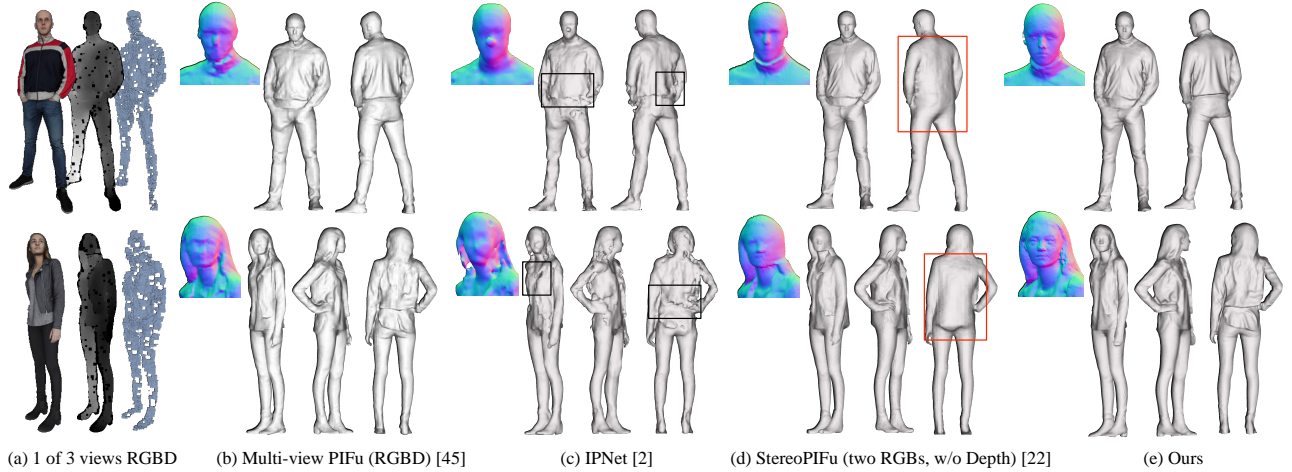


Figure 7. Qualitative comparisons on our testing dataset.

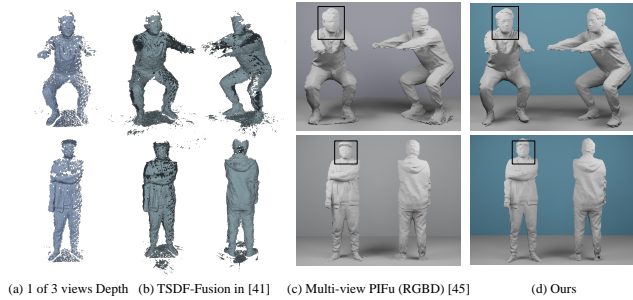


Figure 8. Qualitative comparisons using real depth data.

sor noises on D_{gt} according to [13] to obtain the raw depth map D_{raw} . When training, we sample surface points, volume points according to PIFuHD [46] and obtain their occupancy values as the ground-truth labels. Besides, we randomly select 2 views along with 1 front view from the rendered 60 views of a human scan.

4.1. Comparisons

To evaluate the performance of our method, we compare it with 3 state-of-the-art deep implicit human surface reconstruction methods, including re-implemented PIFu with multi-view RGBD images as input [45], denoted as Multi-view PIFu (RGBD), IPNet (voxelized points cloud as input) [2] and StereoPIFu (stereo RGB images as input) [22]. We retrain the Multi-view PIFu (RGBD) and IPNet on our training dataset for fair comparisons. And we use point-to-surface (P2S) distance(mm), chamfer distance (mm), and MSE for normal map ($1e^{-2}$) as metrics to measure the error between the reconstructed and the ground-truth surfaces on our testing dataset, which contains 106 high-quality models with different poses, clothes, and human-object interactions. The lower metric value means better performance.

Quantitative Comparisons. Tab. 1 reports the comparisons on our testing dataset. It can be seen that our method is ranked as top-1 in both three metrics. Fig. 7 shows two reconstructing results in the testing. Although we use RGBD

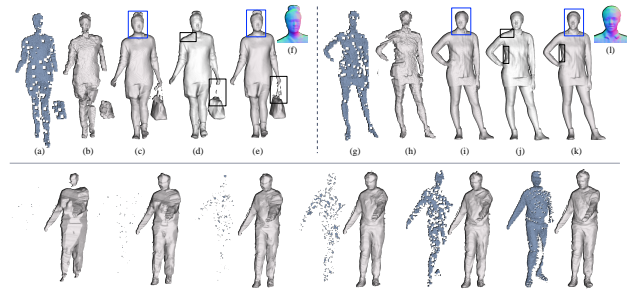


Figure 9. Top row: Visualization of our reconstruction results in the ablation study. (a, g), (b, h), (c, i), (d, j), (e, k), (f, l) are: one-of-three input depth, the results of “w/o DRM”, “w/o PIFu-Face”, “w/o TFA”, ours and our face normal maps. Bottom row: the influence of the degree of noise added to the raw depth map on the reconstruction results. The noise degree is reduced from left to right.

Methods	P2S $\times 10^{-3} \downarrow$	Chamfer $\times 10^{-3} \downarrow$	Normal (MSE) $\times 10^{-2} \downarrow$
Multi-view PIFu (RGBD) [45]	2.988	3.278	1.925
IPNet [2]	3.260	3.152	2.538
StereoPIFu [22]	6.727	7.086	3.415
Ours	2.043	2.235	1.072

Table 1. Quantitative comparisons.

images as inputs for multi-view PIFu, it can not produce reliable results when depth maps contain larger noise. When there is no truncated-PSDF as the input or no attention mechanism for aggregating multi-view features, multi-view PIFu tends to generate over-smooth results, especially for the face. Moreover, the dependence on SMPL initialization limits IPNet to produce reliable results on complex poses. Incorrect SMPL estimation may directly lead to errors in topology. Then, although 3D voxel features based on cost volume can make StereoPIFu achieve better reconstruction results in the front view, the topology error is still obvious when viewed from other perspectives. Besides, 3D cost volume will lead to a heavier network when increasing views. In contrast, our two-scale PIFu improves the local details while maintaining fewer network parameters.

Qualitative Comparisons. Besides the comparisons on

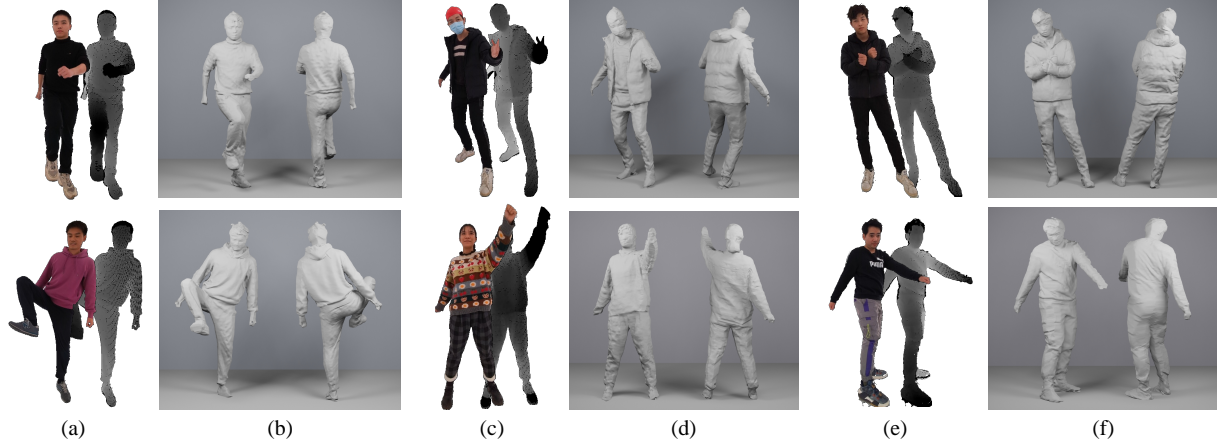


Figure 10. Our reconstruction results with high-fidelity details on real depth data. Columns (a,c,e) show one of the three RGBD inputs. Columns (b,d,f) show our reconstruction results in both front and back views. Note that our method can handle various actions.

the testing dataset illustrated in Fig. 7, we show comparisons on real depth data in Fig. 8. It can be seen that our method can generate results with better face quality (black-box) compared to Multi-view PIFu (RGBD). In addition, TSDF-Fusion cannot generate a complete model due to the very sparse setting of inputs views.

4.2. Ablation Study

We perform ablation studies by removing the model components, including DRM, PIFu-Face, and Transformer-based multi-view feature aggregation (TFA), to better analyze our network’s architecture. The statistics of P2S distance, Chamfer distance, and Normal error are obtained by evaluating the re-trained models on our testing dataset.

Methods	P2S $\times 10^{-3} \downarrow$	Chamfer $\times 10^{-3} \downarrow$	Normal (MSE) $\times 10^{-2} \downarrow$
w/o DRM	17.181	17.093	7.140
w/o PIFu-Face	3.048	3.258	1.412
w/o DRM & PIFu-Face	20.568	21.584	11.295
w/o TFA	2.516	2.579	1.247
Ours	2.043	2.235	1.072

Table 2. Ablation study on our network’s components.

In Tab. 2, we first show that the three modules in our network all contribute to the reconstruction performance. DRM seems to be the most critical component to improve the metric. The reason might be that \mathcal{F}_b in our FBSM only takes the depth maps as inputs only. When our DRM is removed, the noise of the original depth map will directly appear in the results, *e.g.*, (b, h) in Fig. 9. Moreover, as shown in the blue boxes in (c,e,i,k) of Fig. 9, our PIFu-Face significantly improved the geometric details of the face. As for the multiview feature aggregation module, The black boxes in Fig 9 show that directly averaging the multiview features may lead to the loss of some details (*e.g.*, backpack strap) and the jagged-edges at the stitching (d, j). In contrast, adopting self-attention layers can more effectively remove the noises and preserve more body details.

4.3. More Results

We also conduct an experiment to explore our DRM performance by gradually adding different degrees of noise to the raw depth maps. The bottom row of Fig. 9 shows that: even if there is almost no depth information in \mathbf{D}_{raw} , our network can still predict a reasonable reconstruction result based on \mathbf{D}_{rf} . We hypothesize that our DRM is not highly dependent on the depth input, and it owns the ability to predict the depth maps of the whole body due to the joint end-to-end training. Please refer to the supplementary material for more experimental results on our DRM.

Fig. 1 and Fig. 10 show our reconstruction results on real RGBD data and our testing dataset. It can be seen that our reconstruction results can restore the high-fidelity details and the pose of the input body portraits. Furthermore, our facial reconstruction results significantly improved the high-frequency details of the facial features, *e.g.*, eyes, nose, and mouth.

5. Conclusion and Discussion

In this paper, we propose a two-scale PIFu representation to reconstruct the human body and enhance the facial details. The key feature is that we leverage two implicit functions, *i.e.*, PIFu-Body and PIFu-Face, to reduce the modeling complexity. In addition, we designed a DRM for reducing the noise of inputs and a transformer-based feature aggregation module to avoid over-smooth features. After the occupancy-field fusion, our method can generate more reliable, high-fidelity 3D human reconstruction results.

Limitations and Future Work. It remains difficult for our method to handle the cases when the depth noise is significant in high-frequency regions, such as hands and feet. Adding more scales into our two-scale PIFu (refer to Total-Capture [24]) may help to solve this problem. Moreover, our method may not generate facial details when there is occlusion on the face caused by special material (hair, eye-

glasses, etc.) due to the depth error, imposing prior to the facial region may handle this issue. We also plan to investigate the camera setting to improve the quality of reconstructed facial details.

References

- [1] Thiemo Alldieck, Gerard Pons-Moll, Christian Theobalt, and Marcus Magnor. Tex2shape: Detailed full human body geometry from a single image. In *ICCV*, 2019. 2
- [2] Bharat Lal Bhatnagar, Cristian Sminchisescu, Christian Theobalt, and Gerard Pons-Moll. Combining implicit function learning and parametric models for 3d human reconstruction. In *ECCV*, 2020. 2, 7, 12
- [3] Federica Bogo, Michael J. Black, Matthew Loper, and Javier Romero. Detailed full-body reconstructions of moving people from monocular rgb-d sequences. In *ICCV*, 2015. 2
- [4] Derek Bradley, Tiberiu Popa, Alla Sheffer, Wolfgang Heidrich, and Tamy Boubekeur. Markerless garment capture. *ACM TOG*, 2008. 2
- [5] Thomas Brox, Bodo Rosenhahn, Juergen Gall, and Daniel Cremers. Combined region and motion-based 3d tracking of rigid and articulated objects. *IEEE TPAMI*, 2009. 2
- [6] Julian Chibane, Thiemo Alldieck, and Gerard Pons-Moll. Implicit functions in feature space for 3d shape reconstruction and completion. In *CVPR*, 2020. 2
- [7] Alvaro Collet, Ming Chuang, Pat Sweeney, Don Gillett, Dennis Evseev, David Calabrese, Hugues Hoppe, Adam Kirk, and Steve Sullivan. High-quality streamable free-viewpoint video. *ACM TOG*, 2015. 1, 2
- [8] Brian Lee Curless. *New methods for surface reconstruction from range images*. Stanford University, 1997. 3
- [9] Jiankang Deng, Jia Guo, Evangelos Ververas, Irene Kotsia, and Stefanos Zafeiriou. Retinaface: Single-shot multi-level face localisation in the wild. In *Proceedings of the IEEE/CVF Conference on Computer Vision and Pattern Recognition*, pages 5203–5212, 2020. 6
- [10] Mingsong Dou, Philip L. Davidson, S. Fanello, S. Khamis, Adarsh Kowdle, Christoph Rhemann, Vladimir Tankovich, and Shahram Izadi. Motion2fusion: real-time volumetric performance capture. *ACM TOG*, 2017. 2
- [11] Mingsong Dou, Sameh Khamis, Yury Degtyarev, Philip Davidson, Sean Ryan Fanello, Adarsh Kowdle, Sergio Orts Escolano, Christoph Rhemann, David Kim, Jonathan Taylor, et al. Fusion4d: Real-time performance capture of challenging scenes. *ACM TOG*, 2016. 2
- [12] Sai Kumar Dwivedi, Nikos Athanasiou, Muhammed Kocabas, and Michael J. Black. Learning to regress bodies from images using differentiable semantic rendering. In *ICCV*, 2021. 2
- [13] Péter Fankhauser, Michael Bloesch, Diego Rodriguez, Ralf Kaestner, Marco Hutter, and Roland Siegwart. Kinect v2 for mobile robot navigation: Evaluation and modeling. In *2015 International Conference on Advanced Robotics (ICAR)*, pages 388–394. IEEE, 2015. 7
- [14] Valentin Gabeur, Jean-Sébastien Franco, Xavier Martin, Cordelia Schmid, and Gregory Rogez. Moulding humans: Non-parametric 3d human shape estimation from single images. In *ICCV*, 2019. 2
- [15] Juergen Gall, Carsten Stoll, Edilson De Aguiar, Christian Theobalt, Bodo Rosenhahn, and Hans-Peter Seidel. Motion capture using joint skeleton tracking and surface estimation. In *CVPR*, 2009. 2
- [16] Kaiwen Guo, Peter Lincoln, Philip Davidson, Jay Busch, Xueming Yu, Matt Whalen, Geoff Harvey, Sergio Orts-Escolano, Rohit Pandey, Jason Dourgarian, et al. The re-lightables: Volumetric performance capture of humans with realistic relighting. *ACM TOG*, 2019. 1, 2
- [17] Kaiwen Guo, Feng Xu, Yangang Wang, Yebin Liu, and Qionghai Dai. Robust non-rigid motion tracking and surface reconstruction using l0 regularization. In *ICCV*, 2015. 2
- [18] Marc Habermann, Weipeng Xu, Michael Zollhoefer, Gerard Pons-Moll, and Christian Theobalt. Livecap: Real-time human performance capture from monocular video. *ACM TOG*, 2019. 2
- [19] Marc Habermann, Weipeng Xu, Michael Zollhofer, Gerard Pons-Moll, and Christian Theobalt. Deepcap: Monocular human performance capture using weak supervision. In *CVPR*, 2020. 2
- [20] Bharath Hariharan, Pablo Arbeláez, Ross Girshick, and Jitendra Malik. Hypercolumns for object segmentation and fine-grained localization. In *CVPR*, 2015. 3
- [21] Tong He, Yuanlu Xu, Shunsuke Saito, Stefano Soatto, and Tony Tung. Arch++: Animation-ready clothed human reconstruction revisited. In *ICCV*, 2021. 2
- [22] Yang Hong, Juyong Zhang, Boyi Jiang, Yudong Guo, Ligang Liu, and Hujun Bao. Stereopifu: Depth aware clothed human digitization via stereo vision. In *CVPR*, 2021. 1, 7, 12
- [23] Zeng Huang, Yuanlu Xu, Christoph Lassner, Hao Li, and Tony Tung. Arch: Animatable reconstruction of clothed humans. In *CVPR*, 2020. 2
- [24] Hanbyul Joo, Tomas Simon, and Yaser Sheikh. Total capture: A 3d deformation model for tracking faces, hands, and bodies. In *Proceedings of the IEEE conference on computer vision and pattern recognition*, pages 8320–8329, 2018. 2, 8
- [25] Angjoo Kanazawa, Michael J Black, David W Jacobs, and Jitendra Malik. End-to-end recovery of human shape and pose. In *Proceedings of the IEEE conference on computer vision and pattern recognition*, pages 7122–7131, 2018. 1
- [26] Diederik P Kingma and Jimmy Ba. Adam: A method for stochastic optimization. *arXiv preprint arXiv:1412.6980*, 2014. 6
- [27] Muhammed Kocabas, Chun-Hao P. Huang, Joachim Tesch, Lea Müller, Otmar Hilliges, and Michael J. Black. SPEC: Seeing people in the wild with an estimated camera. In *ICCV*, 2021. 2
- [28] Vincent Leroy, Jean-Sébastien Franco, and Edmond Boyer. Multi-view dynamic shape refinement using local temporal integration. In *ICCV*, 2017. 2
- [29] Hao Li, Bart Adams, Leonidas J Guibas, and Mark Pauly. Robust single-view geometry and motion reconstruction. *ACM TOG*, 2009. 2

- [30] Ruilong Li, Yuliang Xiu, Shunsuke Saito, Zeng Huang, Kyle Olszewski, and Hao Li. Monocular real-time volumetric performance capture. In *ECCV*, 2020. 2, 6
- [31] Zhe Li, Tao Yu, Chuanyu Pan, Zerong Zheng, and Yebin Liu. Robust 3d self-portraits in seconds. In *CVPR*, 2020. 2
- [32] Zhe Li, Tao Yu, Zerong Zheng, Kaiwen Guo, and Yebin Liu. Posefusion: Pose-guided selective fusion for single-view human volumetric capture. In *CVPR*, 2021. 2, 3
- [33] Shanchuan Lin, Andrey Ryabtsev, Soumyadip Sengupta, Brian L Curless, Steven M Seitz, and Ira Kemelmacher-Shlizerman. Real-time high-resolution background matting. In *Proceedings of the IEEE/CVF Conference on Computer Vision and Pattern Recognition*, pages 8762–8771, 2021. 3, 6
- [34] Yebin Liu, Qionghai Dai, and Wenli Xu. A point-cloud-based multiview stereo algorithm for free-viewpoint video. *IEEE TVCG*, 2009. 1, 2
- [35] Yebin Liu, Carsten Stoll, Juergen Gall, Hans-Peter Seidel, and Christian Theobalt. Markerless motion capture of interacting characters using multi-view image segmentation. In *CVPR*, 2011. 2
- [36] Matthew Loper, Naureen Mahmood, Javier Romero, Gerard Pons-Moll, and Michael J Black. Smpl: A skinned multi-person linear model. *ACM TOG*, 2015. 1, 2
- [37] Qianli Ma, Jinlong Yang, Siyu Tang, and Michael J. Black. The power of points for modeling humans in clothing. In *ICCV*, 2021. 2
- [38] Armin Mustafa, Hansung Kim, Jean-Yves Guillemaut, and Adrian Hilton. General dynamic scene reconstruction from multiple view video. In *ICCV*, 2015. 2
- [39] Ryota Natsume, Shunsuke Saito, Zeng Huang, Weikai Chen, Chongyang Ma, Hao Li, and Shigeo Morishima. Siclope: Silhouette-based clothed people. In *CVPR*, 2019. 2
- [40] Richard A Newcombe, Dieter Fox, and Steven M Seitz. Dynamicfusion: Reconstruction and tracking of non-rigid scenes in real-time. In *CVPR*, 2015. 1, 2
- [41] Richard A Newcombe, Shahram Izadi, Otmar Hilliges, David Molyneaux, David Kim, Andrew J Davison, Pushmeet Kohi, Jamie Shotton, Steve Hodges, and Andrew Fitzgibbon. Kinectfusion: Real-time dense surface mapping and tracking. In *IEEE ISMAR*, 2011. 1, 2, 4
- [42] Adam Paszke, Sam Gross, Soumith Chintala, Gregory Chanan, Edward Yang, Zachary DeVito, Zeming Lin, Alban Desmaison, Luca Antiga, and Adam Lerer. Automatic differentiation in pytorch. 2017. 6
- [43] Georgios Pavlakos, Vasileios Choutas, Nima Ghorbani, Timo Bolkart, Ahmed A. A. Osman, Dimitrios Tzionas, and Michael J. Black. Expressive body capture: 3d hands, face, and body from a single image. In *CVPR*, pages 10975–10985, 2019. 1, 2
- [44] Gerard Pons-Moll, Sergi Pujades, Sonny Hu, and Michael J Black. Clothcap: Seamless 4d clothing capture and retargeting. *ACM TOG*, 2017. 2
- [45] Shunsuke Saito, Zeng Huang, Ryota Natsume, Shigeo Morishima, Angjoo Kanazawa, and Hao Li. Pifu: Pixel-aligned implicit function for high-resolution clothed human digitization. In *ICCV*, 2019. 1, 2, 6, 7, 12
- [46] Shunsuke Saito, Tomas Simon, Jason Saragih, and Hanbyul Joo. Pifuhd: Multi-level pixel-aligned implicit function for high-resolution 3d human digitization. In *CVPR*, 2020. 1, 2, 6, 7
- [47] D. Smith, M. Loper, X. Hu, P. Mavroidis, and J. Romero. Facsimile: Fast and accurate scans from an image in less than a second. In *ICCV*, 2019. 2
- [48] Zhuo Su, Lan Xu, Zerong Zheng, Tao Yu, Yebin Liu, and Lu Fang. Robustfusion: Human volumetric capture with data-driven visual cues using a rgbd camera. In *ECCV*, 2020. 2
- [49] Yu Sun, Qian Bao, Wu Liu, Yili Fu, Black Michael J., and Tao Mei. Monocular, one-stage, regression of multiple 3d people. In *ICCV*, 2021. 2
- [50] Jing Tong, Jin Zhou, Ligang Liu, Zhigeng Pan, and Hao Yan. Scanning 3d full human bodies using kinects. *IEEE TVCG*, 2012. 1, 2
- [51] Gul Varol, Duygu Ceylan, Bryan Russell, Jimei Yang, Ersin Yumer, Ivan Laptev, and Cordelia Schmid. Bodynet: Volumetric inference of 3d human body shapes. In *ECCV*, 2018. 2
- [52] Ashish Vaswani, Noam Shazeer, Niki Parmar, Jakob Uszkoreit, Llion Jones, Aidan N Gomez, Łukasz Kaiser, and Illia Polosukhin. Attention is all you need. In *Advances in neural information processing systems*, pages 5998–6008, 2017. 5
- [53] Daniel Vlasic, Pieter Peers, Ilya Baran, Paul Debevec, Jovan Popović, Szymon Rusinkiewicz, and Wojciech Matusik. Dynamic shape capture using multi-view photometric stereo. In *ACM SIGGRAPH Asia 2009 papers*, pages 1–11. 2009. 1, 2
- [54] Jingdong Wang, Ke Sun, Tianheng Cheng, Borui Jiang, Chaorui Deng, Yang Zhao, Dong Liu, Yadong Mu, Mingkui Tan, Xinggang Wang, Wenyu Liu, and Bin Xiao. Deep high-resolution representation learning for visual recognition. *IEEE TPAMI*, 43(10):3349–3364, 2021. 5, 6, 13
- [55] Lizhen Wang, Xiaochen Zhao, Tao Yu, Songtao Wang, and Yebin Liu. Normalgan: Learning detailed 3d human from a single rgb-d image. In *ECCV*, 2020. 2
- [56] Shaofei Wang, Marko Mihajlovic, Qianli Ma, Andreas Geiger, and Siyu Tang. Metaavatar: Learning animatable clothed human models from few depth images. In *NeurIPS*, 2021. 2
- [57] Zhou Wang, Alan C Bovik, Hamid R Sheikh, and Eero P Simoncelli. Image quality assessment: from error visibility to structural similarity. *IEEE TIP*, 2004. 4
- [58] Sanghyun Woo, Jongchan Park, Joon-Young Lee, and In So Kweon. Cbam: Convolutional block attention module. In *ECCV*, 2018. 4, 11, 14
- [59] Weipeng Xu, Avishek Chatterjee, Michael Zollhöfer, Helge Rhodin, Dushyant Mehta, Hans-Peter Seidel, and Christian Theobalt. Monoperfcap: Human performance capture from monocular video. *ACM TOG*, 2018. 2
- [60] Shi Yan, Chenglei Wu, Lizhen Wang, Feng Xu, Liang An, Kaiwen Guo, and Yebin Liu. Ddrnet: Depth map denoising and refinement for consumer depth cameras using cascaded cnns. In *ECCV*, 2018. 2, 3, 11, 12
- [61] Genzhi Ye, Yebin Liu, Nils Hasler, Xiangyang Ji, Qionghai Dai, and Christian Theobalt. Performance capture of interacting characters with handheld kinects. In *ECCV*, 2012. 2

- [62] Mao Ye and Ruigang Yang. Real-time simultaneous pose and shape estimation for articulated objects using a single depth camera. In *CVPR*, 2014. 2
- [63] Tao Yu, Zerong Zheng, Kaiwen Guo, Pengpeng Liu, Qionghai Dai, and Yebin Liu. Function4d: Real-time human volumetric capture from very sparse consumer rgbd sensors. In *CVPR*, 2021. 1, 2, 5, 6
- [64] Tao Yu, Zerong Zheng, Kaiwen Guo, Jianhui Zhao, Qionghai Dai, Hao Li, Gerard Pons-Moll, and Yebin Liu. Doublefusion: Real-time capture of human performances with inner body shapes from a single depth sensor. In *CVPR*, 2018. 1, 2
- [65] Tao Yu, Zerong Zheng, Yuan Zhong, Jianhui Zhao, Qionghai Dai, Gerard Pons-Moll, and Yebin Liu. Simulcap: Single-view human performance capture with cloth simulation. In *CVPR*, 2019. 2
- [66] Yebin Liu Zerong Zheng, Tao Yu and Qionghai Dai. Pamir: Parametric model-conditioned implicit representation for image-based human reconstruction. *IEEE TPAMI*, 2021. 2
- [67] Jason Y Zhang, Sam PePOSE, Hanbyul Joo, Deva Ramanan, Jitendra Malik, and Angjoo Kanazawa. Perceiving 3d human-object spatial arrangements from a single image in the wild. In *European Conference on Computer Vision*, pages 34–51. Springer, 2020. 1
- [68] Hang Zhao, Orazio Gallo, Iuri Frosio, and Jan Kautz. Loss functions for neural networks for image processing. *arXiv:1511.08861*, 2015. 4
- [69] Yang Zheng, Ruizhi Shao, Yuxiang Zhang, Tao Yu, Zerong Zheng, Qionghai Dai, and Yebin Liu. Deepmulticap: Performance capture of multiple characters using sparse multiview cameras. In *IEEE Conference on Computer Vision (ICCV 2021)*, 2021. 5
- [70] Zerong Zheng, Tao Yu, Yixuan Wei, Qionghai Dai, and Yebin Liu. Deephuman: 3d human reconstruction from a single image. In *ICCV*, 2019. 2, 6
- [71] Hao Zhu, Xinxin Zuo, Sen Wang, Xun Cao, and Ruigang Yang. Detailed human shape estimation from a single image by hierarchical mesh deformation. In *CVPR*, 2019. 2
- [72] Michael Zollhöfer, Matthias Nießner, Shahram Izadi, Christoph Rehmann, Christopher Zach, Matthew Fisher, Chenglei Wu, Andrew Fitzgibbon, Charles Loop, Christian Theobalt, et al. Real-time non-rigid reconstruction using an rgb-d camera. *ACM TOG*, 2014. 2

Supplementary Material. Overview

In this supplementary material, we mainly report the details of the network parameters of our depth refinement module (DRM) in Sec. A, perform more experiments to evaluate our DRM performance (Sec. B), evaluate the effectiveness of our face-to-body occupancy fields fusion (Sec. C) and the process of obtaining our RGBD real data (Sec. D). Finally, we show more reconstruction results (Sec. E) using our proposed method.

A. The Network Structure Details of DRM

In Tab. A, we report the detailed parameters of the CBAM-ResBlock [58] used in our DRM. Moreover, Tab. B illustrates the overall structure of our DRM. The input resolution of our DRM is 512×512 during training and testing, where the input depth map \mathbf{D}_{raw} of DRM is the normalized result of the original depth map \mathbf{D}_{ori} via the formulation: $\mathbf{D}_{raw} = (\mathbf{D}_{ori} - z_{center})/z_{size}$. The z_{center} and z_{size} during training are set to 1.8m and 1m respectively since we place the camera 1.8m away from the person to be photographed and suppose that length of the body bounding-box is 2m when generating the training data. Similarly, we set z_{center} and z_{size} to 1.5m and 1m respectively when testing on real RGBD images. Since the noise value 0 appeared in \mathbf{D}_{raw} is mapped to $-z_{center}/z_{size}$, which will introduce additional factors, i.e., z_{center} and z_{size} to our DRM, we choose to clip \mathbf{D}_{raw} to $[-1, 1]$ to avoid these factors. In other words, 0 will be mapped to -1 no matter how far away the camera is from the human body. This operation will make our DRM more robust to the input depth map. For the output \mathbf{D}_{rf} of our DRM, we first use $Tanh$ to map \mathbf{D}_{rf} to $[-1, 1]$, then unnormalize \mathbf{D}_{rf} by: $\mathbf{D}_{rf} = \mathbf{D}_{rf} * z_{size} + z_{center}$. Afterward, we use the binary mask \mathbf{M} to set the background value of \mathbf{D}_{rf} to 0, so that the background does not participate in training.

B. Evaluation of Depth Refinement Module

To further evaluate the performance of our DRM, we first compare it with the state-of-the-art method DDRNet [60], which includes a depth denoising network and a depth refinement network. We use their pre-trained model and evaluate it on our testing dataset and real RGBD data. As illustrated in Fig. A, our DRM can more effectively refine the raw depth maps with holes and eroded boundaries compared to DDRNet, resulting in better reconstruction performance. Besides, since we did not re-train DDRNet on our training dataset, this may cause their results to be still full of noise on our testing dataset.

Secondly, to verify whether our differentiable surface reconstruction module, i.e., FBSM benefits our DRM in the end-to-end training, we conduct an experiment by detaching the output \mathbf{D}_{rf} of the DRM. In this way, the DRM will not be supervised by the FBSM. As shown in Fig. B, we can see that, during jointly training, the loss terms L_{depth} (in our DRM) and L_O (in our FBSM) drop faster than those of detaching \mathbf{D}_{rf} , especially between epoch 4 and 23, and finally converge to lower values ($8.61e^{-4}$ vs. $9.61e^{-4}$, 0.0986 vs. 0.0992). These results show that under the supervision of FBSM with the ground-truth 3D data, our DRM can learn the depth information of the whole body better, and benefit FBSM in obtaining better reconstruction results from \mathbf{D}_{rf} .

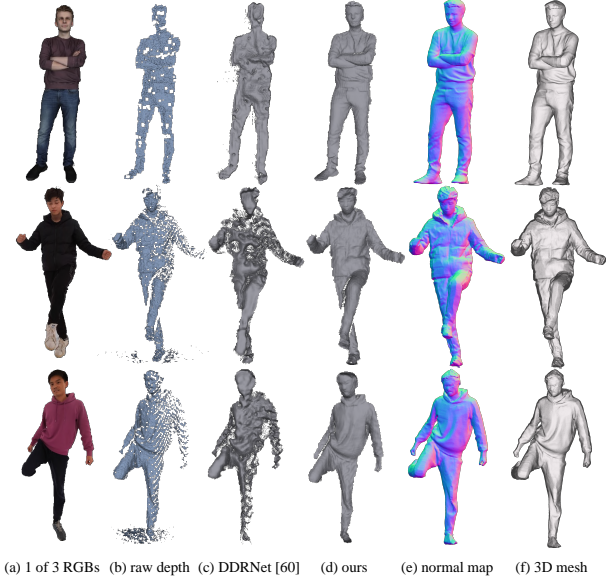


Figure A. Our DRM vs. DDRNet [60] First row: an example from our testing dataset. Last two rows: examples using real RGBD images

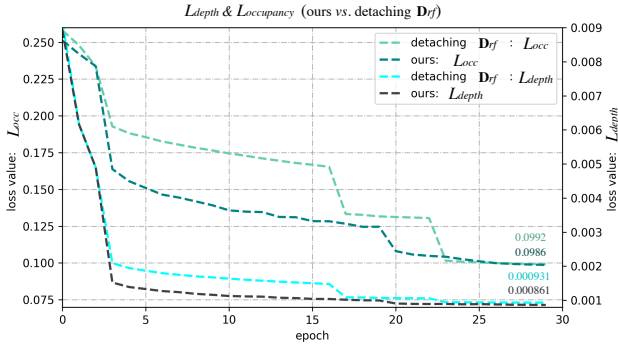


Figure B. The convergence curves of loss terms L_{depth} and L_O during training. (Ours vs. detaching D_{rf} in the DRM). Note that L_{depth} and L_O are the average losses in each epoch.

C. Evaluation of Occupancy Fields Fusion

We conduct an ablation study by removing the *face-to-body occupancy fields fusion* in our FBSM. As a result, the occupancy values of the 3D points projected on the face region will be independently predicted by the face MLP. As shown in Fig. C, when the occupancy fields fusion operation is removed, the geometric noise and errors appeared on the back of the head and the marginal areas of the face (black-boxes) can be seen clearly. In contrast, our complete approach can generate results with less noise in these regions.

Since the PIFu-Face \mathcal{F}_f in our FBSM is trained only on the sampling points near the face region for learning facial geometry. For those points far away from but projected on the facial region, \mathcal{F}_f will not be able to generate reasonable occupancy prediction values. Then, it is necessary to perform occupancy field fusion on those points to eliminate errors.

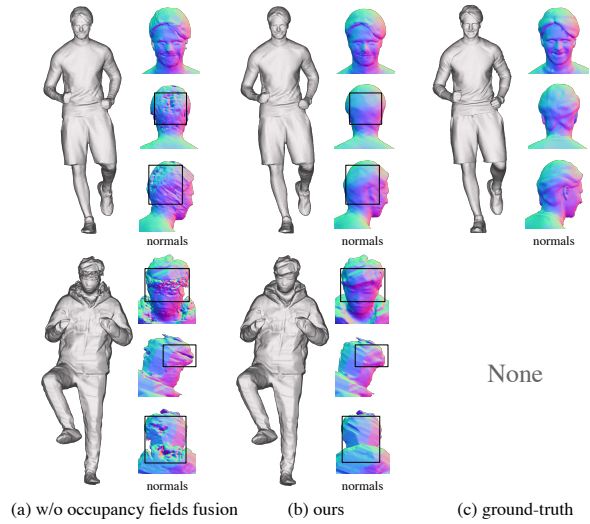


Figure C. The effect of face-to-body occupancy fields fusion. Last row: evaluation using real RGBD images.

D. The Process of Obtaining Real RGBD Data

In the capturing stage, we placed 8 groups of color and depth (KinectV4 sensors) cameras in a circle at 45-degree intervals to ease the calibration, 4 groups of photography lights at 90-degree intervals to provide uniform illumination, as illustrated in Fig. D.a. For each camera, we used the infrared calibration board to calibrate the intrinsic parameters and initial extrinsic Kinect camera parameters. Then we used the iterative closest point (ICP) method to match the points clouds captured by multiple depth sensors to further optimize the extrinsic parameters. Afterward, we recorded the captured RGBD images and performed the de-distortion operation on the captured RGB images. When testing on these real RGBD images, we will select three-view RGBD images with intervals of (135 degree, 135 degree, 90 degree) as shown in Fig. D.b, and the user is required to face the camera in the middle.

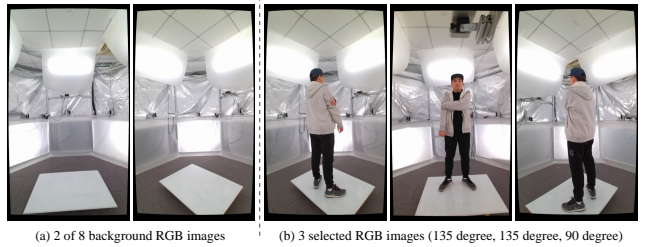


Figure D. Our capturing system.

E. More Results

In this section, we first show more qualitative comparison results between ours and 3 state-of-the-art learning-based human reconstruction methods (*i.e.*, PIFu [45], IP-Net [2], StereoPIFu [22]). As shown in Fig. E, our method can reconstruct high fidelity 3D human models at both front

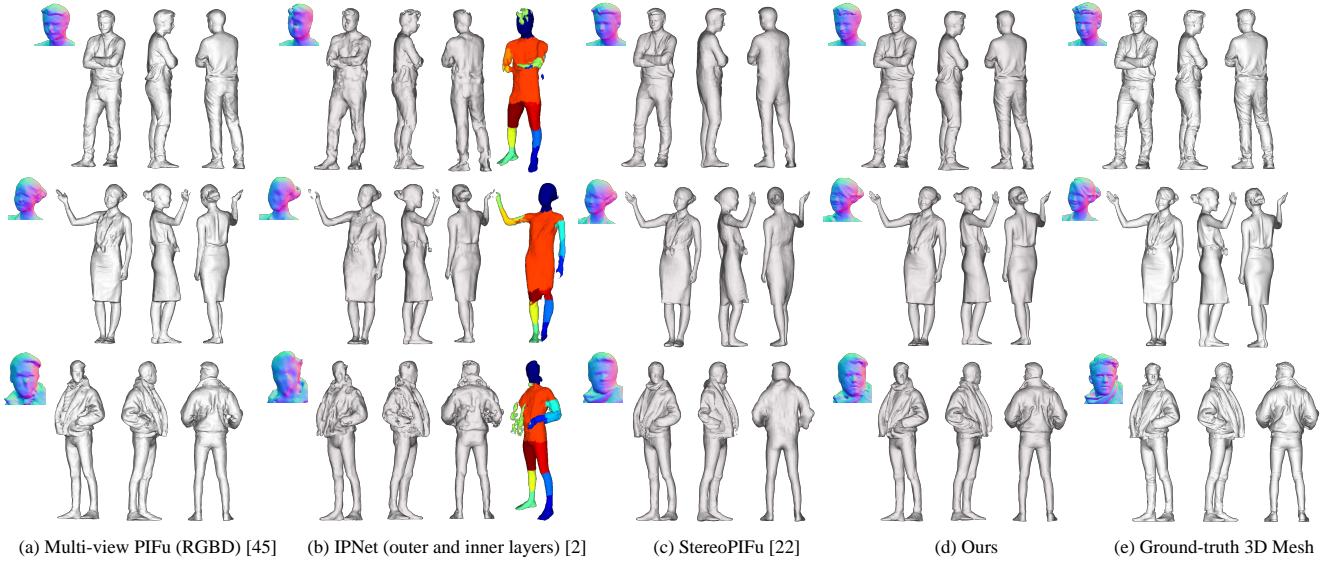


Figure E. Qualitative comparisons on our testing dataset.

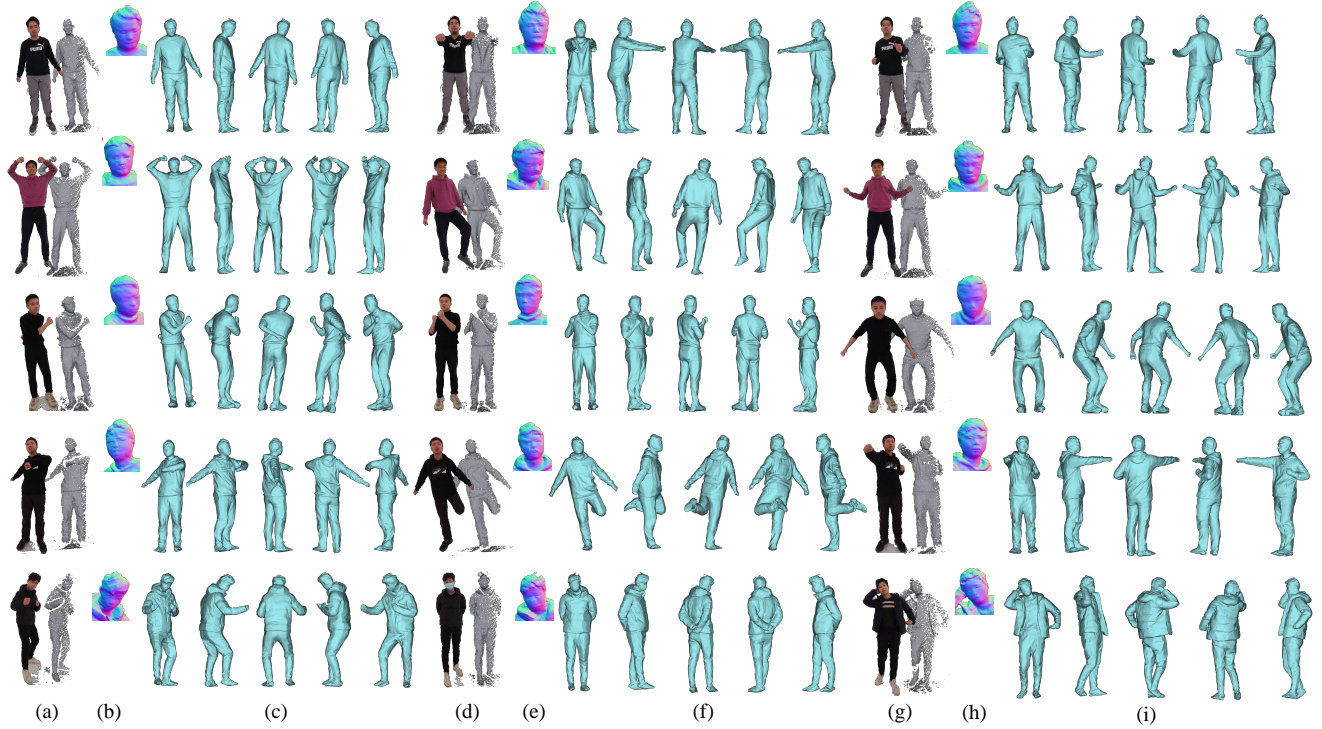


Figure F. More reconstruction results on real RGBD images. Columns (a, d, g) show one-view RGBD inputs. Columns (b, e, h) show the face normal maps in the front-view. Columns (c, f, i) show our reconstruction results of five views (with an interval of 72 degrees).

and back side of the model and 3D faces with more details. For the comparison with multi-view PIFu (RGBD), we also use HRNetV2-W18-Small-v2 [54] as the backbone (with the same setting as \mathcal{H}_b in our PIFu-Body) but set the number of input channels to 4 to facilitate the input of RGBD data. Besides, we show more reconstruction results with our network on real RGBD images in Fig. F.

Block name	Output size	Filter size or Setting
CBAM-ResBlock [58]		
Conv_1 + ReLU	$H \times W \times C$	$3 \times 3, C, \text{stride}=1$
Conv_2	$H \times W \times C$	$3 \times 3, C, \text{stride}=1$
CBAM-Layer		
Channel-attention (Shared MLP)		
AdaptiveAvgPool2d	$1 \times 1 \times C$	Input: output of Conv_2, Pooling output size: 1×1
Conv_2 + ReLU	$1 \times 1 \times (C/2)$	$1 \times 1, C/2$ (reduction=2), stride=1
Conv_3	$1 \times 1 \times C$	$1 \times 1, C, \text{stride}=1$
AdaptiveMaxPool2d	$1 \times 1 \times C$	Input: output of Conv_2, Pooling output size: 1×1
Conv_2 + ReLU	$1 \times 1 \times (C/2)$	$1 \times 1, C/2$ (reduction=2), stride=1
Conv_3	$1 \times 1 \times C$	$1 \times 1, C, \text{stride}=1$
Add + Sigmoid_1	$1 \times 1 \times C$	Inputs: two outputs of Conv_3
Spatial-attention		
Mean	$H \times W \times 1$	Input: output of Conv_2, keep_dim=True
Max	$H \times W \times 1$	Input: output of Conv_2, keep_dim=True
Concat + Conv_4 + Sigmoid_2	$H \times W \times 1$	Inputs: output of Mean and Max, $7 \times 7, 1, \text{stride}=1$
Multiplication_1	$H \times W \times C$	Inputs: output of Sigmoid_1, input of Conv_1
Multiplication_2	$H \times W \times C$	Inputs: output of Multiplication_1, output of Sigmoid_2
Add	$H \times W \times C$	Inputs: output of Multiplication_2, input of Conv_1

Table A. The detailed parameters of CBAM-ResBlocks [58]. The dimension of the input feature map is $H \times W \times C$. The variable reduction is set to 2 in this table.

Block name	Output size	Filter size or Setting
Encoder (two branches for Depth: D_{raw} and RGB: I)		
Conv1_d + LeakyReLU	$H \times W \times 32$	Input: Depth, $7 \times 7, \text{stride}=1, \text{padding}=3$
Conv1_c + LeakyReLU	$H \times W \times 32$	Input: RGB, $7 \times 7, \text{stride}=1, \text{padding}=3$
Add_1	$H \times W \times 32$	Inputs: output of Conv1_d and Conv1_c
Conv2_c + LeakyReLU	$(H/2) \times (W/2) \times 64$	$3 \times 3, \text{stride}=2, \text{padding}=1$
Conv2_d + LeakyReLU	$(H/2) \times (W/2) \times 64$	Input: output of Add_1, $3 \times 3, \text{stride}=2, \text{padding}=1$
Conv3_d + LeakyReLU	$(H/2) \times (W/2) \times 64$	$3 \times 3, \text{stride}=1, \text{padding}=1$
Add_2	$(H/2) \times (W/2) \times 64$	Inputs: output of Conv3_d and Conv2_c
Conv3_c + LeakyReLU	$(H/4) \times (W/4) \times 128$	$3 \times 3, \text{stride}=2, \text{padding}=1$
Conv4_d + LeakyReLU	$(H/4) \times (W/4) \times 128$	Input: output of Add_2, $3 \times 3, \text{stride}=2, \text{padding}=1$
Conv5_d + LeakyReLU	$(H/4) \times (W/4) \times 128$	$3 \times 3, \text{stride}=1, \text{padding}=1$
Conv6_d + LeakyReLU	$(H/4) \times (W/4) \times 128$	$3 \times 3, \text{stride}=1, \text{padding}=1$
Add_3	$(H/4) \times (W/4) \times 128$	Inputs: output of Conv6_d and Conv3_c
(diConv_i + LeakyReLU) $\times 4$	$(H/4) \times (W/4) \times 128$	$3 \times 3, \text{stride}=1, \text{padding}=\{2,4,8,16\}, \text{dilation}=\{2,4,8,16\}$
CBAM-ResBlock ($C=128, \text{reduction}=8$) $\times 2$, (Tab. A)		
Add_4	$(H/4) \times (W/4) \times 128$	Inputs: output of Add_3 and the last CBAM-ResBlock
Decoder (additional input: the RGB binary mask M)		
deconv1 + AvgPool + LeakyReLU	$(H/2) \times (W/2) \times 64$	$4 \times 4, \text{stride}=2, \text{padding}=1, \text{pooling}: 2 \times 2, \text{stride}=1$
Add_5	$(H/2) \times (W/2) \times 64$	Inputs: output of Add_2 and output of last LeakyReLU
Conv7 + LeakyReLU	$(H/2) \times (W/2) \times 64$	$3 \times 3, \text{stride}=1, \text{padding}=1$
deconv2 + AvgPool + LeakyReLU	$H \times W \times 32$	$4 \times 4, \text{stride}=2, \text{padding}=1, \text{pooling}: 2 \times 2, \text{stride}=1$
Add_6	$H \times W \times 32$	Inputs: output of Add_1 and output of last LeakyReLU
Conv8 + LeakyReLU	$H \times W \times 16$	$3 \times 3, \text{stride}=1, \text{padding}=1$
Conv8 + Tanh	$H \times W \times 1$	$3 \times 3, \text{stride}=1, \text{padding}=1$
Multiply	$H \times W \times 1$	Input: the binary mask M and output of Tanh
Add_7	$H \times W \times 1$	Inputs: output of Multiply and $-(1 - M)$

Table B. The detailed network structure of our depth refinement module. The dimensions of the input RGB I , Depth D_{raw} , Mask M are denoted as $H \times W \times 3, H \times W \times 1$ and $H \times W \times 1$, respectively.